Available online at www.sciencedirect.com
ScienceDirect
Nuclear Instruments and Methods in Physics Research A 584 (2008) 418–423
NUCLEAR INSTRUMENTS & METHODS IN PHYSICS RESEARCH Section A
www.elsevier.com/locate/nima

Multiple imaging radiography at LNLS

M.G. Hönnicke[a,*], C. Cusatis[a], A. Antunes[b], A.M.V. Safatle[c], P.S.M. Barros[c], S.L. Morelhão[b]

[a]LORXI, Departamento de Física, Universidade Federal do Paraná, Caixa Postal 19091, 81531-990 Curitiba, PR, Brazil
[b]Departamento de Física Aplicada, Instituto de Fisica, Universidade de São Paulo, Caixa Postal 66318, 05315-970 São Paulo, SP, Brazil
[c]Laboratório de Oftalmologia Experimental e Comparativa, Departamento de Cirurgia, Faculdade de Medicina Veterinária, Universidade de São Paulo, 05508-900 São Paulo, Brazil

Received 15 August 2007; received in revised form 23 October 2007; accepted 23 October 2007
Available online 20 November 2007

Abstract

An analyzer-based X-ray phase-contrast imaging (ABI) setup has been mounted at the Brazilian Synchrotron Light Laboratory (LNLS) for multiple imaging radiography (MIR) purposes. The algorithm employed for treating the MIR data collected at LNLS is described, and its reliability in extracting the distinct types of contrast that can be obtained with MIR is demonstrated by analyzing a test sample (thin polyamide wire). As a practical application, the possibility of studying ophthalmic tissues, corneal sequestra in this case, via MIR is investigated.
© 2007 Elsevier B.V. All rights reserved.

PACS: 07.85.Qe; 87.59.Bh; 87.59.−e

Keywords: X-ray imaging; Diffraction-enhanced imaging; X-ray phase-contrast imaging

1. Introduction

Phase-contrast X-ray imaging is a well-established technique that has been employed in many fields of knowledge, such as biology [1], materials science [2], medical sciences [3,4], and archeology [5]. It reveals structural details of the samples that are invisible to conventional radiography. Several methods are reported in the literature to acquire phase-contrast images: (1) X-ray wave propagation method, which uses either monochromatic [2,6] or partially coherent polychromatic [7] X-ray sources; (2) methods based on X-ray interferometry [8–10] and (3) analyzer-based imaging (ABI) methods [11–15] where the X-ray beam transmitted through the sample is diffracted in a highly perfect crystal (known as the analyzer crystal) prior to detection. Hence, ABI methods require monochromatic and non-dispersive (+, −) [16] X-ray beams instead of high-coherence sources.

X-ray absorption, refraction, and ultra-small angle scattering (USAXS) are the three main features resulting from radiation–matter interaction processes to which ABI methods are sensitive to. By rocking the analyzer crystal through the Bragg diffraction condition, it is possible to enhance selectively each one of these features, since they occur at distinct angular ranges. However, their contributions in the acquired images of the diffracted beam still appear overlapped, even at different angular positions of the analyzer's rocking curve (RC). To extract the exact amount of absorption, refraction, and scattering taking place as the beam crosses the sample, multiple images acquired as a function of the RC angle are, therefore, needed for further processing via deconvolution algorithms. In high-flux synchrotron sources where several images can be quickly recorded, a linear deconvolution algorithm, known as the diffraction-enhanced imaging (DEI), has been used in a geometric optics approximation, where the intensity variation during the RC is considered to be linear with the angular displacement of the beam [15,17]. In other words, the line-profile function of the RC

*Corresponding author. Tel./fax: +55 41 32669271.
E-mail address: marcelohonnicke@yahoo.com.br (M.G. Hönnicke).

0168-9002/$ - see front matter © 2007 Elsevier B.V. All rights reserved.
doi:10.1016/j.nima.2007.10.036

is taken by a triangular one. This linear behavior has been replaced for more realistic ones in improved versions of the DEI algorithms [18–21]. Moreover, even more sophisticated algorithms for processing multiple images from analyzer-based techniques have been proposed by Nesterets et al. [22,23] and Pavlov et al. [24] accounting for other minor details, such as phase modulation due to objects, diffraction in all crystals along the beam path, effects of wave propagation in free space, polychromaticity of the source and its finite size.

In the present work, the improved DEI algorithm proposed by Rigon et al. [19] was implemented for analyzing images collected at the Brazilian Synchrotron Light Laboratory (LNLS). This algorithm requires only three images to be taken at specific positions of the RC, and this fact makes it very attractive for being used with relative low-flux X-ray sources. Quantitative studies have been carried out with a thin polyamide wire by comparing measured and simulated images. Moreover, the algorithm was also applied for treating images of corneal sequestra. The possibilities of studying ophthalmic diseases related to this particular tissue are discussed.

2. Experiment

ABI has been carried out with the experimental setup schematized in Fig. 1, and characterized in details elsewhere [25]. The non-dispersive four-crystal ABI setup [26] consists of two symmetrical Si 333 channel-cuts, one as the first crystal positioned prior to the sample and the other as the analyzer crystal. Rotation of both channel-cuts are motor controlled by a double-axis diffractometer of very good thermo-mechanical stability and resolution of 0.3 μrad/step [27]. X-ray photon energy was set to 10.7 keV by a double-crystal Si 111 beamline monochromator. Beamline mirrors and the sagital focusing monochromator have been adjusted to aim, as much as possible, a parallel beam in both vertical and horizontal scattering planes; measured divergences in this near-parallel-beam configuration were 40 and 600 μrad, respectively. Beamsize, at the sample position, is $0.7 \times 20\,mm^2$ (vertical × horizontal). During image acquisition, coupled vertical translators scan both sample and detector simultaneously in front of the beam; the total scan range is 25 mm. Conventional synchrotron attenuation radiographs were taken with the sample placed after the analyzer crystals and very close to the CCD detector, which has 1242×1152 pixels of $22.5 \times 22.5\,\mu m^2$ each.

3. Quantitative studies

Fig. 1(b) shows the analyzer's RC carried out before placing the sample in between the two channel-cut crystals. The three images necessary to use the deconvolution algorithm [19] were taken at the positions indicated by numbers 1 (slope minus), 2 (vicinity of the top), and 3 (slope plus) in Fig. 1(b). For quantitative studies, a 300-μm-thick polyamide wire has been used as a test sample, and the set of multiple images collected at the above mentioned positions is shown in Fig. 2(a)–(c), while, for sake of comparison, the corresponding simulated images are provided in Fig. 2(d)–(f).

Simulated images are obtained by a geometrical optics approach within the plane wave approximation where the incoming monochromatic beam is attenuated and refracted by the sample; it is a procedure similar to that used by Protopopov and Kalnov [28]. To predict the images at the positions 1, 2, and 3 of the RC, its line-profile function is taken into account by a Gaussian function of 7 μrad full-width at half-maximum (FWHM). Hence, the theoretical intensity at each pixel is predicted by the following procedure: (1) the angular deviations of the beam on each spatial position of the sample (corresponding to a pixel size) are calculated by using the Snell law; (2) the computed deflections in the beam directions are convoluted with the Gaussian function; and (3) the final calculation is to multiply these intensity values with the percentage of attenuation (linear absorption) in each pixel of the image. This simulation procedure was found to be suitable when

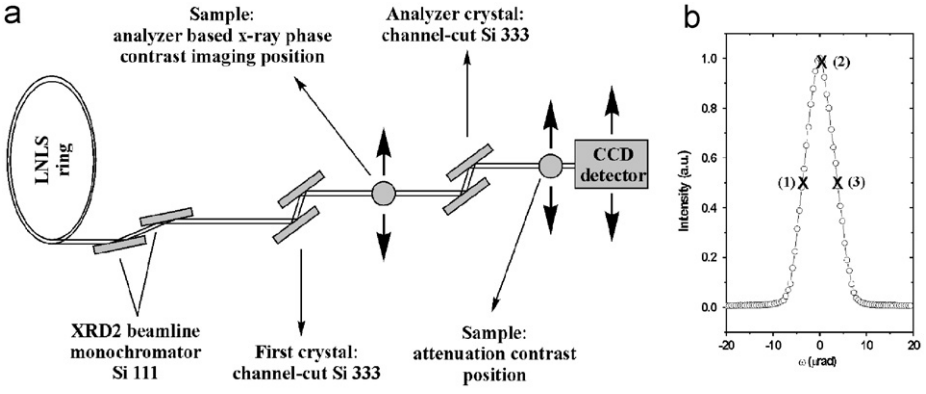

Fig. 1. (a) Non-dispersive (+, −) ABI setup at the XRD2 beamline at LNLS (10.7 keV). (b) Analyzer Si 333 rocking curve (RC) and the angular positions 1–3 where the images were acquired.

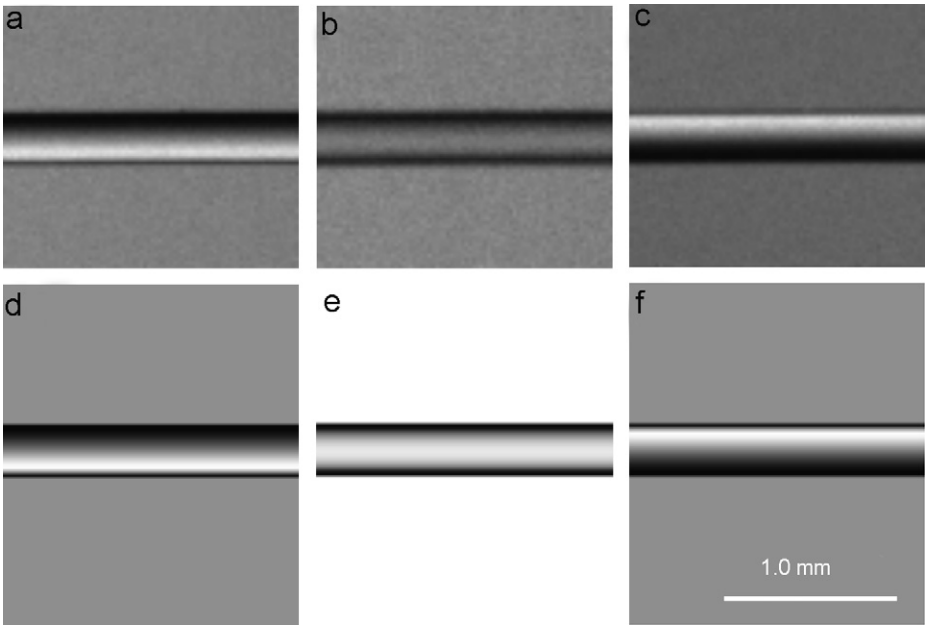

Fig. 2. (a–c) Measured AB images of a polyamide wire acquired on the slope minus, vicinity of the top, and slope plus of the RC (positions 1, 2, and 3, respectively, in Fig. 1(b)). (d–f) Simulated AB images of the same polyamide wire (300 μm thick) for the same angular positions of the RC where the measured ABIs were acquired.

comparing the measured and simulated images, as shown in Fig. 2.

To apply the improved DEI algorithm for treating each set of three images, either experimental or simulated, values of reflectivity, R_α ($\alpha = 1$, 2, and 3), as well as of their first and second derivatives, $\dot{R}_\alpha$ and $\ddot{R}_\alpha$, at the RC positions where the images were taken, are necessary. From the RC in Fig. 1(b), we have that $R_\alpha = [0.5 \quad 0.99 \quad 0.5]$, $\dot{R}_\alpha = [0.85 \quad -0.38 \quad -0.85]$, and $\ddot{R}_\alpha = [0.054 \quad -3.19 \quad 0.054]$. With these values in hands, the intensities I_α at each pixel of image α were processed in a MATLAB code, according to the Rigon et al. equations [19]:

$$I_A = \frac{I_1(\dot{R}_2\ddot{R}_3 - \ddot{R}_2\dot{R}_3) - I_2(\dot{R}_1\ddot{R}_3 - \ddot{R}_1\dot{R}_3) + I_3(\dot{R}_1\ddot{R}_2 - \ddot{R}_1\dot{R}_2)}{R_1(\dot{R}_2\ddot{R}_3 - \ddot{R}_2\dot{R}_3) - R_2(\dot{R}_1\ddot{R}_3 - \ddot{R}_1\dot{R}_3) + R_3(\dot{R}_1\ddot{R}_2 - \ddot{R}_1\dot{R}_2)}, \tag{1}$$

$$I_R = -\frac{I_1(R_2\ddot{R}_3 - \ddot{R}_2R_3) - I_2(R_1\ddot{R}_3 - \ddot{R}_1R_3) + I_3(R_1\ddot{R}_2 - \ddot{R}_1R_2)}{I_1(\dot{R}_2\ddot{R}_3 - \ddot{R}_2\dot{R}_3) - I_2(\dot{R}_1\ddot{R}_3 - \ddot{R}_1\dot{R}_3) + I_3(\dot{R}_1\ddot{R}_2 - \ddot{R}_1\dot{R}_2)}, \tag{2}$$

and

$$I_S = 2\frac{I_1(R_2\dot{R}_3 - \dot{R}_2R_3) - I_2(R_1\dot{R}_3 - \dot{R}_1R_3) + I_3(R_1\dot{R}_2 - \dot{R}_1R_2)}{I_1(\dot{R}_2\ddot{R}_3 - \ddot{R}_2\dot{R}_3) - I_2(\dot{R}_1\ddot{R}_3 - \ddot{R}_1\dot{R}_3) + I_3(\dot{R}_1\ddot{R}_2 - \ddot{R}_1\dot{R}_2)} - (I_R)^2, \tag{3}$$

where I_A, I_R, and I_S are the pixel intensities in the apparent absorption, refraction, and USAXS images, respectively. These treated images are shown in Fig. 3 as obtained from the two sets of images in Fig. 2.

Discrepancies between USAXS images (Fig. 3(c) and (f)) arise because the wire does not present microstructures. Experimental and simulated images of apparent absorption and refraction were found to be consistent as can be seen by comparing Fig. 3(a) and (d) and Fig. 3(b) and (e). The former comparison shows almost the same combination of absorption and refraction at the wire border; and the latter shows similar gradients in the refraction index as well as some not expected effects, such as the dark contrast at the top of the simulated image. A possible explanation relies on the very small angular width of the RC that is smaller than the deviations of the beam when crossing a sample and/or the combination of free-space propagation and ABI effects as previously reported by Pavlov et al. [24] and Coan et al. [29]. This can be the limitation of the algorithm employed here, as also discussed elsewhere [19].

4. Qualitative studies

Ophthalmologic diseases have been studied by using, among other techniques, the ABI [30–32]. The ABI proved to be useful to identify different structures in healthy and diseased (with cataract) crystalline lenses [30,31]. Also, microcalcifications were found in experiments developed with higher energies [32].

Herein, to test the improved DEI algorithm [19] with the measurements acquired at LNLS, ABIs of a corneal sequestra tissue were acquired. Studies of the corneal matrix structures have been done by small-angle X-ray scattering [33,34], but never with X-ray imaging. Also, the corneal sequestra has been studied by several authors in the literature [35–38]. This disease is common in felines (Persian cats are predisposed to this condition) and is typified by the brown to black discoloration of the cornea. However, the cause of this disease is not completely

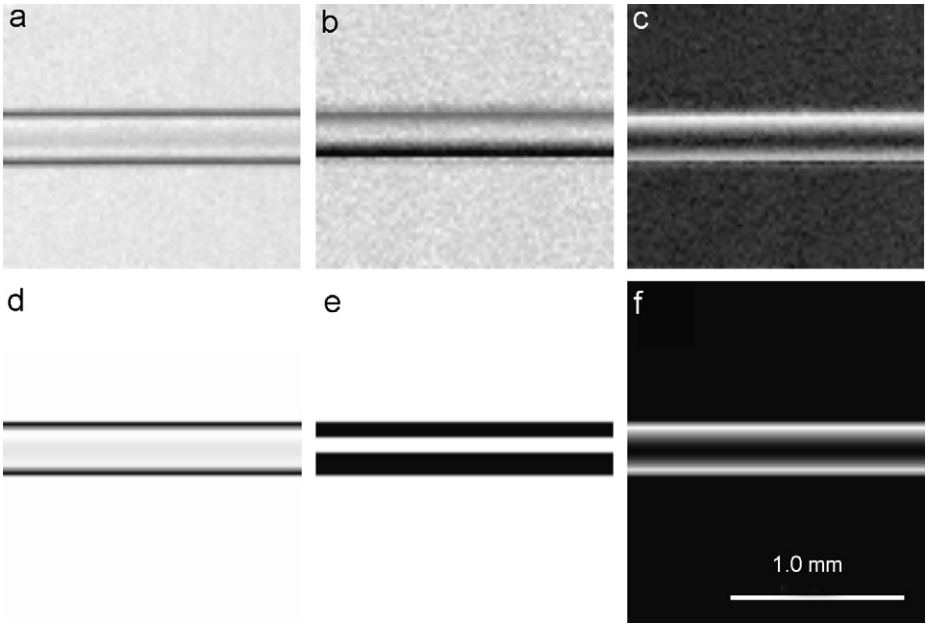

Fig. 3. (a–c) Apparent absorption image, refraction image, and USAXS image, respectively, of the same polyamide wire shown in Fig. 2. Such images were obtained by using the measured images from Fig. 2 and Eqs. (1)–(3). (d–f) Simulated images: apparent absorption image, refraction image, and USAXS image, respectively. Such images were obtained by using the simulated AB images (Fig. 2(d)–(f)) and Eqs. (1)–(3).

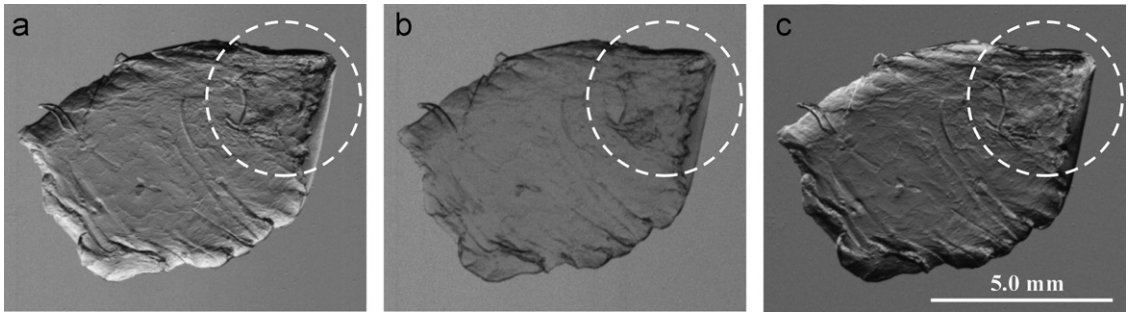

Fig. 4. (a–c) AB corneal sequestra images acquired on the slope minus, vicinity of the top, and slope plus of the rocking curve (RC) (positions 1, 2, and 3, respectively, in Fig. 1(b)), respectively.

established. It may be hereditary, or caused by the incorrect palpebral closure, or caused by a defect in the lachrymal secretion, or due to a herpes virus infection. Moreover, the changes in the cornea microstructure due to such a disease is not well knowledged. For this reason, a corneal sequestra tissue was imaged here to try to identify structures in the lesionated area (discolorated area) that cannot be detected with other techniques, but could be detected with X-rays. The sequestra tissue was surgically obtained by a lamellar keratectomy of a Persian cat. The ABIs of this tissue are shown in Fig. 4, where the lesionated area is selected by dashed circles. These images were used to obtain the DEI images with the improved algorithm. The lesionated area is more emphasized in the refraction angle and USAXS images (shown by dashed circles in Fig. 5) because they can be correlated to clusters of melanin particles found in such area, as reported in the literature [33], and/or to the mineralization and fibrosis that is already known as mineralized corneal sequestra [34].

5. Conclusions

An improved DEI algorithm has been used to treat images acquired with a standard ABI setup working at 10.7 keV. The algorithm was found to be useful for the acquired data with a limitation for the large analyzer RC widths when compared to the deviations of the beam. This limitation was checked by measured and simulated images of a thin polyamide wire. However, the algorithm proved to be very good to find structures in a corneal sequestra tissue that can be correlated to the particles of melanin and/or mineralization and fibrosis found in the diseased part of the cornea.

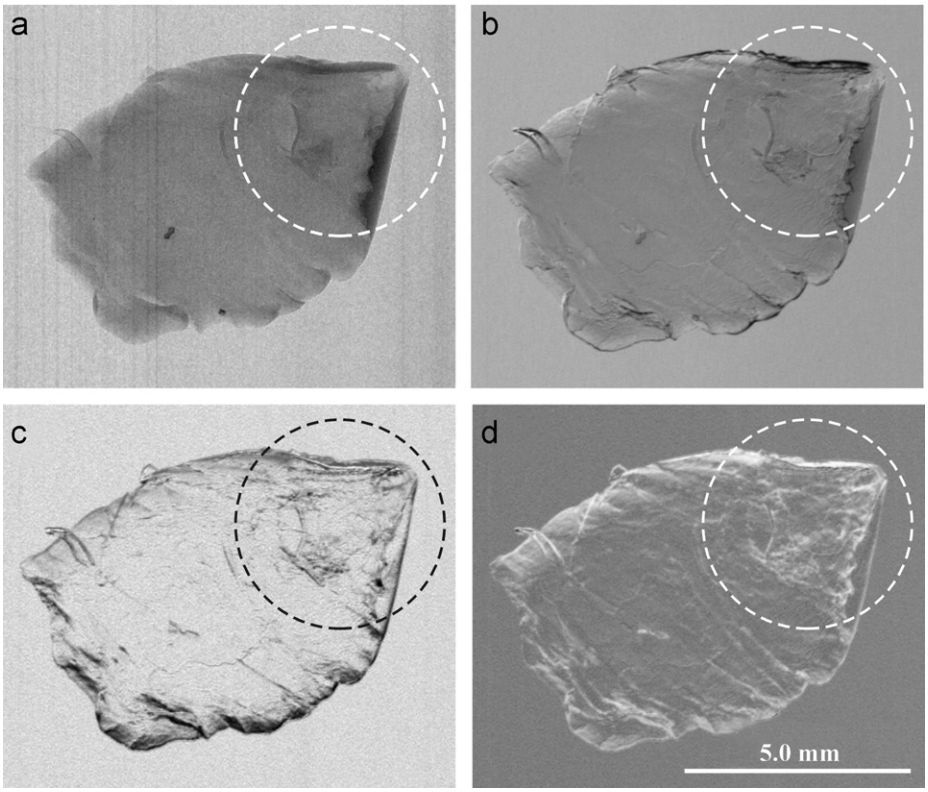

Fig. 5. (a–d) Conventional synchrotron radiography, apparent absorption image, refraction image, and USAXS image, respectively, of the same corneal sequestra tissue shown in Fig. 4. The dashed circles show the lesionated area.

Acknowledgments

The authors are grateful to LNLS/MCT (proposals D10A-3417/2005 and D10A-3561/2005), PRONEX/CNPq/Fundacao Araucaria, and CNPq for the financial support. M.G. Hönnicke is grateful to CNPq/PDJ for the fellowship. The authors also acknowledge the beamline staff Guinther Kellerman for his scientific assistance previous and during the experiment and Rubens C. da Silva for the help in the experiment preparation.

References

[1] M.W. Wesneat, O. Betz, R.W. Blob, K. Fezzaa, W.J. Cooper, W.-K. Lee, Science 299 (2003) 558.
[2] P. Cloetens, M. Pateyron-Salome, J.Y. Buffiere, G. Peix, J. Baruchel, F. Peyrin, M. Schlenker, J. Appl. Phys. 81 (1997) 5878.
[3] R.E. Johnston, D. Washburn, E. Pisano, C. Burns, W.C. Thomlinson, L.D. Chapman, F. Arfelli, N.F. Gmur, Z. Zhong, D. Sayers, Radiology 200 (3) (1996) 659.
[4] J. Li, Z. Zhong, R. Lidtke, K.E. Kuettner, C. Peterfy, E. Aliyeva, C. Muehleman, J. Anat. 202 (5) (2003) 463.
[5] Y. Chaimanee, D. Jolly, M. Benammi, P. Tafforeau, D. Duzer, I. Moussa, J.J. Jaeger, Nature 422 (2003) 61.
[6] A. Snigirev, I. Snigireva, V. Kohn, S. Kuznetsov, I. Schelokov, Rev. Sci. Instrum. 66 (1995) 5486.
[7] S.W. Wilkins, T.E. Gureyev, D. Gao, A. Pogany, A.W. Stevenson, Nature 384 (1996) 335.
[8] M. Ando, S. Hosoya, An attempt at X-ray phase-contrast microscopy, in: G. Shinoda, et al. (Eds.), Proceedings of the 6th International Conference on X-Ray Optics and Microanalysis, University of Tokyo Press, Tokyo, 1972, p. 63.
[9] F. Pfeifer, T. Weitkamp, O. Bunk, C. David, Nature Phys. 2 (2006) 258.
[10] F. Pfeiffer, C. Kottler, O. Bunk, C. David, Phys. Rev. Lett. 98 (2007) 108105.
[11] E. Förster, K. Goetz, P. Zaumseil, Krist. Tech. 15 (1980) 937.
[12] K.M. Podurets, V.A. Somenkov, S.Sh. Shilśhtein, Sov. Phys. Tech. Phys. 34 (6) (1989) 654.
[13] V.N. Ingal, E.A. Beliaevskaya, J. Phys. D 28 (1995) 2314.
[14] T.J. Davis, D. Gao, T.E. Gureyev, A.W. Stevenson, S.W. Wilkins, Nature 373 (1995) 595.
[15] D. Chapman, W. Thomlinson, R.E. Johnston, D. Washburn, E. Pisano, N. Gmür, Z. Zhong, R. Menk, F. Arfelli, D. Sayers, Phys. Med. Biol. 42 (1997) 2015.
[16] J.W.M. Dumond, Phys. Rev. 52 (1937) 872.
[17] M.O. Hasnah, C. Parham, E.D. Pisano, Z. Zhong, O. Oltulu, D. Chapman, Med. Phys. 32 (2005) 549.
[18] L. Rigon, H.J. Besch, F. Arfelli, R.H. Menk, G. Heitner, H. Plotow-Besch, J. Phys. D 36 (10A) (2003) A107.
[19] L. Rigon, F. Arfelli, R.-H. Menk, Appl. Phys. Lett. 90 (2007) 114102.
[20] E. Pagot, P. Cloetens, S. Fiedler, A. Bravin, P. Coan, J. Baruchel, J. Hartwig, W. Thomlinson, Appl. Phys. Lett. 82 (20) (2003) 3421.
[21] O. Oltulu, Z. Zhong, M. Hasnah, M.N. Wernick, D. Chapman, J. Phys. D 36 (17) (2003) 2152.
[22] Ya.I. Nesterets, T.E. Gureyev, D. Paganin, K.M. Pavlov, S.W. Wilkins, J. Phys. D 37 (2004) 1262.
[23] Ya.I. Nesterets, T.E. Gureyev, S.W. Wilkins, J. Phys. D 38 (2005) 4259.
[24] K.M. Pavlov, T.E. Gureyev, D. Paganing, Ya.I. Nesterets, M.J. Morgan, R.A. Lewis, J. Phys. D 37 (2004) 2746.

[25] M.G. Hönnicke, G. Kellerman, H.S. Rocha, C. Giles, G. Tirao, I. Mazzaro, R.T. Lopes, C. Cusatis, Rev. Sci. Instrum. 76 (2005) 093703.
[26] U. Bonse, M. Hart, Z. Phys. 189 (2) (1966) 151.
[27] M. Hart, Characterization of crystal growth defects by X-ray methods, in: B.K. Tanner, D.K. Bowen (Eds.), NATO Advanced Study Institutes Series, Series B: Physics, Plenum Press, New York, 1980, p. 484.
[28] V.V. Protopopov, V.A. Kalnov, Opt. Commun. 184 (2000) 1.
[29] P. Coan, E. Pagot, S. Fiedler, P. Cloetens, J. Baruchel, A. Bravin, J. Synchrotron Radiat. 12 (2005) 241.
[30] A. Antunes, M.G. Hönnicke, C. Cusatis, S.L. Morelhão, J. Phys. D 38 (10A) (2005) A85.
[31] A. Antunes, M.G. Hönnicke, A.M.V. Safatle, C. Cusatis, P.S.M. Barros, S.L. Morelhão, Nucl. Instr. and Meth. B 238 (1–4) (2005) 28.
[32] A. Antunes, A.M.V. Safatle, P.S.M. Barros, S.L. Morelhão, Med. Phys. 33 (7) (2006) 2338.
[33] G.F. Elliot, J.M. Goodfellow, A.E. Woolgar, P.A. Timmins, J. Appl. Crystallogr. 11 (1978) 496.
[34] A.J. Quantock, C. Boote, R.D. Young, S. Hayes, H. Tanioka, S. Kawasaki, O. Noboru, T. Lida, N. Yagi, K. Shigeru, K.M. Meek, J. Appl. Crystallogr. 40 (2007) s335.
[35] S.E. Andrew, S. Tou, D.E. Brooks, Vet. Ophthalmol. 4 (2) (2001) 107.
[36] M.B. Glaze, Clin. Tech. Small Anim. Pract. 20 (2) (2005) 74.
[37] H.J. Featherstone, V.J. Franklin, J. Sansom, Vet. Ophthalmol. 7 (4) (2004) 229.
[38] A.J. Gemenski, D.A. Wilkie, J. Am. Vet. Med. Assoc. 219 (11) (2001) 1568.